

Efficient Approximation of Jacobian Matrices Involving a Non-Uniform Fast Fourier Transform (NUFFT)

Guanhua Wang and Jeffrey A. Fessler

Abstract—There is growing interest in learning Fourier domain sampling strategies (particularly for MRI) using optimization approaches. For non-Cartesian sampling patterns, the system models typically involve non-uniform FFT (NUFFT) operations. Commonly used NUFFT algorithms contain frequency domain interpolation, which is not differentiable with respect to the sampling pattern, complicating the use of gradient methods. This paper describes an efficient and accurate approach for computing approximate gradients involving NUFFTs. Multiple numerical experiments validated the improved accuracy and efficiency of the proposed approximation. As an application to computational imaging, the NUFFT Jacobians were used to optimize non-Cartesian MRI sampling trajectories via data-driven stochastic optimization. Specifically, the sampling patterns were learned with respect to various model-based reconstruction algorithms, including quadratic regularized reconstruction and compressed sensing-based reconstruction. The proposed approach enables sampling optimization for image sizes that are infeasible with standard auto-differentiation methods due to memory limits. The synergistic acquisition and reconstruction lead to remarkably improved image quality. In fact, we show that model-based image reconstruction (MBIR) methods with suitably optimized imaging parameters can perform nearly as well as CNN-based methods.

Index Terms—NUFFT, auto-differentiation, MRI k-space trajectory, accelerated MRI, data-driven optimization, machine learning

I. INTRODUCTION

There are several computational imaging modalities where the raw measurements can be modeled as samples of the imaged object’s spectrum, where those samples need not lie on the Cartesian grid, including radar [1], diffraction ultrasound tomography [2], parallel-beam tomography [3], and magnetic resonance imaging (MRI) [4], [5]. Image reconstruction methods for such modalities may use non-uniform fast Fourier transform (NUFFT) operations to accelerate computation [6], [7]. The quality of the reconstructed image depends both on the image reconstruction method and on the characteristics of the frequency domain sampling pattern. MRI has particular flexibility in designing the k-space sampling patterns, and many methods were proposed to find optimal sampling schemes [8], [9], [10], [11], [12], [13]. Recently there has been growing interest in learning k-space sampling patterns for MRI using data-driven optimization approaches inspired

by machine learning methods, for both Cartesian [14], [15], [16], [17], [18] and non-Cartesian [19], [20], [21] cases.

The non-Cartesian sampling pattern is a collection of continuous points in k-space, so its optimization is amenable to gradient-based methods, though it is also possible to apply derivative-free optimization algorithms [22], [23]. To learn a non-Cartesian k-space sampling pattern from image-domain training data using gradient methods, one may solve an optimization problem involving both the forward model for the MRI system and the image reconstruction method, both of which depend on NUFFT operations. In principle, the Fourier transform operation is a continuous function of the k-space sample locations and thus should be applicable to gradient-based optimization methods. In practice, the NUFFT ($\mathcal{O}(N \log N)$) is an approximation to the non-uniform discrete Fourier transform (NUDFT, $\mathcal{O}(N^2)$) and that approximation often is implemented using non-differentiable lookup table operations or other interpolation techniques [24], [25]. Such approximations are sufficient for image reconstruction, but are problematic if one attempts to use standard auto-differentiation tools for gradient-based optimization due to efficiency and accuracy. Standard auto-differentiation methods using subgradients can lead to incorrect NUFFT Jacobians. They also require prohibitively large amounts of memory for back-propagation through certain algorithm stages such as conjugate gradient (CG) steps that involve NUFFT operations.

This paper takes an efficient approach that replaces memory-intensive and inaccurate auto-differentiation steps with fast Jacobian approximations that are themselves based on NUFFT operations. Notably, the proposed approach requires much lower memory for iterative updates like CG steps.

As a direct application, we used the proposed Jacobian in learning MRI sampling trajectories via stochastic optimization. By applying the forward system model and subsequent reconstruction, reconstructed images were simulated from reference images in the training set. The similarity between simulated and reference images is the metric for updating the sampling trajectory. Notably, the reconstruction here is model-based (including but not limited to least-squares and compressed sensing). In comparison with previous works using reconstruction neural networks (NN) [19], [21], such model-based reconstruction methods can be more robust and require less training data. Compared to the bilevel optimization approach [18], the proposed method is more versatile since it is not limited to smooth and convex regularizers.

In addition to simple NUFFT-based sensing matrices, we

This work supported in part by NIH Grants R01 EB023618 and U01 EB026977 and NSF Grant IIS 1838179.

G. Wang is with the Department of Biomedical Engineering, University of Michigan, Ann Arbor, MI 48109 USA (e-mails:guanhuaw@umich.edu).

J. A. Fessler is with the Department of EECS, University of Michigan, Ann Arbor, MI 48109 USA (e-mail:fessler@umich.edu).

also considered some practical scenarios in MR sampling and reconstruction, including the multi-coil (sensitivity-encoded) [26] and \mathbf{B}_0 -informed system model [27]. The derivation also includes the fast Jacobian approximation for Gram and “data consistency” operations commonly used in iterative reconstruction methods.

Jacobians with respect to the non-Cartesian sampling pattern are also relevant for tomographic image reconstruction problems with unknown view angles (like cryo-EM) where the view angles must be estimated [28].

The methods in this paper were used to assist the design of k-space sampling for a CNN-based reconstruction approach in our previous work [21]. This paper derives the theory in detail and considers k-space sampling optimization for general model-based reconstruction methods. Preliminary results were shown in an earlier conference short abstract [29].

The remainder of this paper is organized as follows. Section II derives the efficient Jacobian approximations. Section III details how to optimize MRI sampling patterns using learning-based methods. Section IV provides empirical validation of the approach, showing the efficacy and accuracy of the proposed approach.

II. JACOBIAN EXPRESSIONS

This section derives the key Jacobian expressions and their efficient approximations based on NUFFT operations. These approximations are the key to enabling the applications that follow.

A. Notation

We denote matrices, vectors and scalars by \mathbf{A} , \mathbf{a} and a , respectively. \mathbf{A}' , \mathbf{A}^T and \mathbf{A}^* denote the Hermitian transpose, the transpose and the complex conjugate of \mathbf{A} , respectively.

For Jacobian matrices, we follow the “numerator-layout” notation¹. For example, the derivative of an m -element column vector \mathbf{y} w.r.t. an n -element vector \mathbf{x} is an $m \times n$ matrix:

$$\frac{\partial \mathbf{y}}{\partial \mathbf{x}} \triangleq \begin{bmatrix} \frac{\partial y_1}{\partial x_1} & \frac{\partial y_1}{\partial x_2} & \cdots & \frac{\partial y_1}{\partial x_n} \\ \frac{\partial y_2}{\partial x_1} & \frac{\partial y_2}{\partial x_2} & \cdots & \frac{\partial y_2}{\partial x_n} \\ \vdots & \vdots & \ddots & \vdots \\ \frac{\partial y_m}{\partial x_1} & \frac{\partial y_m}{\partial x_2} & \cdots & \frac{\partial y_m}{\partial x_n} \end{bmatrix}. \quad (1)$$

However, this convention does not handle scenarios such as the derivatives of the elements of one matrix w.r.t the elements of another matrix. Thus, we adopt a natural extension by using the vec (vectorization) operation. Specifically, for a $M \times N$ matrix \mathbf{A} that is a function of a $P \times Q$ matrix \mathbf{B} , we write the derivative as a $MN \times PQ$ matrix by applying (1) to the vec of each matrix:

$$\mathcal{D}_{\mathbf{B}} \mathbf{A} = \mathcal{D}_{\mathbf{B}} \mathbf{A}(\mathbf{B}) \triangleq \frac{\partial \text{vec}(\mathbf{A})}{\partial \text{vec}(\mathbf{B})}. \quad (2)$$

This note uses Wirtinger derivatives for solving complex derivatives. Consider a complex-valued function $f(z)$, Wirtinger derivatives calculate gradients of $\frac{\partial f}{\partial z}$ and $\frac{\partial f}{\partial z^*}$ to

enable differentiating non-holomorphic functions. For holomorphic functions, $\frac{\partial f}{\partial z^*} = 0$ [30].

The following equalities are useful in our derivations. (The equalities that involve products all assume the sizes are compatible.) For $\mathbf{A} \in \mathbb{C}^{K \times L}$, $\mathbf{B} \in \mathbb{C}^{L \times M}$, $\mathbf{C} \in \mathbb{C}^{M \times N}$:

$$\begin{aligned} \text{vec}(\mathbf{ABC}) &= (\mathbf{I}_N \otimes \mathbf{AB}) \text{vec}(\mathbf{C}) \\ &= (\mathbf{C}^T \mathbf{B}^T \otimes \mathbf{I}_K) \text{vec}(\mathbf{A}). \end{aligned} \quad (P1)$$

In general:

$$(\mathbf{A} \otimes \mathbf{B})(\mathbf{C} \otimes \mathbf{D}) = (\mathbf{AC}) \otimes (\mathbf{BD}). \quad (P2)$$

For $\mathbf{A} \in \mathbb{C}^{K \times L}$, $\mathbf{B} \in \mathbb{C}^{M \times N}$:

$$\mathbf{A} \otimes \mathbf{B} = (\mathbf{I}_K \otimes \mathbf{B})(\mathbf{A} \otimes \mathbf{I}_N) = (\mathbf{A} \otimes \mathbf{I}_M)(\mathbf{I}_L \otimes \mathbf{B}). \quad (P3)$$

For $\mathbf{A} \in \mathbb{C}^{M \times N}$, $\mathbf{x} \in \mathbb{C}^N$:

$$\mathcal{D}_{\mathbf{A}}(\mathbf{Ax}) = \mathbf{x}^T \otimes \mathbf{I}_M, \quad \mathcal{D}_{\mathbf{A}^*}(\mathbf{Ax}) = \mathbf{0} \quad (P4)$$

Finally we have:

$$\begin{aligned} \mathbf{A} \in \mathbb{C}^{N \times N} \implies \mathcal{D}_{\mathbf{A}} \mathbf{A}^{-1} &= -(\mathbf{A}^T)^{-1} \otimes \mathbf{A}^{-1}, \\ \mathcal{D}_{\mathbf{A}^*} \mathbf{A}^{-1} &= \mathbf{0}. \end{aligned} \quad (P5)$$

The chain rule still holds for the extended Jacobian formulation. Suppose $F : \mathbb{C}^{K \times L} \rightarrow \mathbb{C}^{M \times N}$ and $G : \mathbb{C}^{M \times N} \rightarrow \mathbb{C}^{P \times Q}$ are holomorphic. For $\mathbf{X} \in \mathbb{C}^{K \times L}$, the Jacobian of the composite function is:

$$\underbrace{\mathcal{D}_{\mathbf{X}} G(F(\mathbf{X}))}_{PQ \times KL} = \underbrace{\mathcal{D}_{\mathbf{Y}} G(\mathbf{Y})|_{\mathbf{Y}=F(\mathbf{X})}}_{PQ \times MN} \underbrace{\mathcal{D}_{\mathbf{X}} F(\mathbf{X})}_{MN \times KL}. \quad (P6)$$

Equalities (P1)-(P3) are common matrix vectorization properties. See [31, Ch. 9] for (P4), [32] for (P5) and (P6).

B. System Model

Consider the (single-coil, initially) MRI measurement model for non-Cartesian sampling based on the NUDFT [5]:

$$\mathbf{y} = \mathbf{Ax} + \boldsymbol{\varepsilon},$$

where $\mathbf{y} \in \mathbb{C}^M$ denotes the measured k-space data, $\mathbf{x} \in \mathbb{C}^N$ denotes the unknown image to be reconstructed, and $\mathbf{A} \in \mathbb{C}^{M \times N}$ denotes the system matrix or encoding matrix, where $\mathbf{A} = \mathbf{A}(\boldsymbol{\omega})$ has elements

$$a_{ij} = e^{-i\vec{\omega}_i \cdot \vec{r}_j}, \quad i = 1, \dots, M, \quad j = 1, \dots, N \quad (3)$$

for $\vec{\omega}_i \in \mathbb{R}^D$ and $\vec{r}_j \in \mathbb{R}^D$ where $D \in \{1, 2, 3, \dots\}$ denotes the image dimension, and where

$$\boldsymbol{\omega} = [\boldsymbol{\omega}^{[1]} \ \boldsymbol{\omega}^{[2]} \ \dots \ \boldsymbol{\omega}^{[D]}]$$

is the $M \times d$ matrix consisting of all the k-space sampling locations and $\boldsymbol{\omega}^{[d]} \in \mathbb{R}^M$ denotes its d th column. (For simplicity here, we ignore other physical effects like field inhomogeneity and relaxation that are sometimes included in the forward model in MRI [5].) The voxel center locations $\{\vec{r}_j\}$ usually lie on a Cartesian grid, but the k-space sample locations $\boldsymbol{\omega}$ in principle can be arbitrary subject to the Nyquist constraint that $|\vec{\omega}_i \cdot \vec{r}_j| < \pi$.

Typically \mathbf{A} is approximated by a NUFFT [6]. Usually, the NUFFT operator involves frequency-domain interpolation

¹See https://en.wikipedia.org/wiki/Matrix_calculus#Numerator-layout_notation.

operations that are often non-differentiable. One previous trajectory optimization approach that used auto-differentiation [19] replaced the non-differentiable lookup table with a bilinear interpolation operation. Bilinear interpolation is differentiable everywhere except at the sample locations. Auto-differentiation of bilinear interpolation involves differentiating some `floor` and `ceiling` operations and those derivatives are defined to be zero in popular deep learning frameworks such as PyTorch and TensorFlow, leading to suboptimal sub-gradient calculations. Nearest-neighbor interpolation has even worse properties for auto-differentiation because its derivative is zero almost everywhere, leading to a completely vanishing gradient.

In the following derivations, we investigate a different approach where we analyze (on paper) the gradients w.r.t. ω and \mathbf{x} , using the (NUDFT) expression (3), and then implement that expression efficiently using NUFFT approximations. This approach enables faster computation and requires much less memory.

C. Forward Operator

We first focus on the forward operation $\mathbf{A}(\omega) \mathbf{x}$ and determine Jacobian matrices with respect to \mathbf{x} and ω . The $M \times N$ Jacobian matrix of the forward operation with respect to \mathbf{x} is simply \mathbf{A} itself:

$$\frac{\partial \mathbf{A} \mathbf{x}}{\partial \mathbf{x}} = \mathbf{A}, \quad \frac{\partial \mathbf{A} \mathbf{x}}{\partial \mathbf{x}^*} = \mathbf{0}.$$

For the d th column of ω :

$$\begin{aligned} \left[\frac{\partial \mathbf{A} \mathbf{x}}{\partial \omega^{[d]}} \right]_{il} &= \frac{\partial [\mathbf{A} \mathbf{x}]_i}{\partial \omega_l^{[d]}} \\ &= \frac{\partial}{\partial \omega_l^{[d]}} \sum_{j=1}^N e^{-i\bar{\omega}_i \cdot \bar{r}_j} x_j \\ &= \begin{cases} -i \sum_{j=1}^N e^{-i\bar{\omega}_i \cdot \bar{r}_j} x_j r_j^{[d]}, & i = l \\ 0, & \text{otherwise,} \end{cases} \end{aligned}$$

for $i, l = 1, \dots, M$. The above summation is the product of the i th row of \mathbf{A} with $\mathbf{x} \odot \mathbf{r}^{[d]}$. Thus the $M \times M$ Jacobian matrix for the partial derivatives of $\mathbf{A} \mathbf{x}$ w.r.t. $\omega^{[d]}$ is:

$$\frac{\partial \mathbf{A} \mathbf{x}}{\partial \omega^{[d]}} = -i \text{diag} \left\{ \mathbf{A}(\mathbf{x} \odot \mathbf{r}^{[d]}) \right\}. \quad (4)$$

Consequently, the Jacobian calculation should apply \mathbf{A} to vector $\mathbf{x} \odot \mathbf{r}^{[d]}$ once. In the above derivation, \mathbf{A} is a NUFFT operator. In the practical implementation, we use a NUFFT to approximate \mathbf{A} , both for the forward model and for the Jacobian calculation.

D. Adjoint Operator

Derivations of the Jacobians for the adjoint operation $\mathbf{A}'(\omega) \mathbf{y}$ follow a similar approach. For \mathbf{y} :

$$\frac{\partial \mathbf{A}' \mathbf{y}}{\partial \mathbf{y}} = \mathbf{A}', \quad \frac{\partial \mathbf{A}' \mathbf{y}}{\partial \mathbf{y}^*} = \mathbf{0}.$$

For the d th column of ω , the $N \times M$ Jacobian matrix has elements:

$$\begin{aligned} \left[\frac{\partial \mathbf{A}' \mathbf{y}}{\partial \omega^{[d]}} \right]_{jl} &= \frac{\partial [\mathbf{A}' \mathbf{y}]_j}{\partial \omega_l^{[d]}} \\ &= \frac{\partial \sum_{i=1}^M e^{i\bar{\omega}_i \cdot \bar{r}_j} y_i}{\partial \omega_l^{[d]}} \\ &= i e^{i\bar{\omega}_i \cdot \bar{r}_j} y_i r_j^{[d]}. \end{aligned}$$

Thus the Jacobian matrix is

$$\frac{\partial \mathbf{A}' \mathbf{y}}{\partial \omega^{[d]}} = i \text{diag} \left\{ \mathbf{r}^{[d]} \right\} \mathbf{A}' \text{diag} \left\{ \mathbf{y} \right\}. \quad (5)$$

Again, to apply this Jacobian to a vector \mathbf{v} efficiently, we apply the NUFFT adjoint \mathbf{A}' to $\mathbf{v} \odot \mathbf{y}$, and then scale by $i \mathbf{r}^{[d]}$.

E. Gram Matrix

The product $\mathbf{A}'(\omega) \mathbf{A}(\omega) \mathbf{x}$ of the Gram matrix of the NUFFT with a vector also arises optimization steps and requires appropriate Jacobian matrices. For \mathbf{x} :

$$\frac{\partial \mathbf{A}' \mathbf{A} \mathbf{x}}{\partial \mathbf{x}} = \mathbf{A}' \mathbf{A}, \quad \frac{\partial \mathbf{A}' \mathbf{A} \mathbf{x}}{\partial \mathbf{x}^*} = \mathbf{0}.$$

The (k, j) th element of the $N \times N$ matrix containing the partial derivatives of the Gram matrix w.r.t. $\omega_l^{[d]}$ is

$$\begin{aligned} \left[\frac{\partial \mathbf{A}' \mathbf{A}}{\partial \omega_l^{[d]}} \right]_{k,j} &= \frac{\partial}{\partial \omega_l^{[d]}} \sum_{i=1}^M e^{-i\bar{\omega}_i \cdot (\bar{r}_j - \bar{r}_k)} \\ &= -i (r_j^{[d]} - r_k^{[d]}) e^{-i\bar{\omega}_i \cdot (\bar{r}_j - \bar{r}_k)} \\ &= -i (r_j^{[d]} - r_k^{[d]}) a_{lk}^* a_{lj}. \end{aligned} \quad (6)$$

In matrix form:

$$\frac{\partial \mathbf{A}' \mathbf{A}}{\partial \omega_l^{[d]}} = i \text{diag} \left\{ \mathbf{r}^{[d]} \right\} \mathbf{A}' \mathbf{e}_l \mathbf{e}_l' \mathbf{A} - i \mathbf{A}' \mathbf{e}_l \mathbf{e}_l' \mathbf{A} \text{diag} \left\{ \mathbf{r}^{[d]} \right\}. \quad (7)$$

When multiplying the Jacobian with a vector \mathbf{x} :

$$\begin{aligned} \frac{\partial \mathbf{A}' \mathbf{A}}{\partial \omega_l^{[d]}} \mathbf{x} &= i \text{diag} \left\{ \mathbf{r}^{[d]} \right\} \mathbf{a}_l (\mathbf{a}_l' \mathbf{x}) - i \mathbf{a}_l \mathbf{a}_l' \text{diag} \left\{ \mathbf{r}^{[d]} \right\} \mathbf{x} \\ &= i (\mathbf{a}_l' \mathbf{x}) (\mathbf{r}^{[d]} \odot \mathbf{a}_l) - i (\mathbf{a}_l' (\mathbf{x} \odot \mathbf{r}^{[d]})) \mathbf{a}_l, \end{aligned} \quad (8)$$

where $\mathbf{a}_l = \mathbf{A}' \mathbf{e}_l$ denotes the l th column of \mathbf{A}' .

Consider the extended Jacobian expression:

$$\mathcal{D}_{\omega_l^{[d]}} \mathbf{A}' \mathbf{A} = \text{vec} \left(\frac{\partial \mathbf{A}' \mathbf{A}}{\partial \omega_l^{[d]}} \right).$$

Multiplying by \mathbf{x} yields:

$$\begin{aligned} \frac{\partial \mathbf{A}' \mathbf{A}}{\partial \omega_l^{[d]}} \mathbf{x} &= \text{vec} \left(\frac{\partial \mathbf{A}' \mathbf{A}}{\partial \omega_l^{[d]}} \mathbf{x} \right) \\ &= (\mathbf{x}^T \otimes \mathbf{I}_N) \text{vec} \left(\frac{\partial \mathbf{A}' \mathbf{A}}{\partial \omega_l^{[d]}} \right) \quad (\text{use P1}) \\ &= (\mathbf{x}^T \otimes \mathbf{I}_N) \left(\mathcal{D}_{\omega_l^{[d]}} \mathbf{A}' \mathbf{A} \right) \\ &= (\mathcal{D}_{\mathbf{A}' \mathbf{A}} \mathbf{A}' \mathbf{A} \mathbf{x}) \left(\mathcal{D}_{\omega_l^{[d]}} \mathbf{A}' \mathbf{A} \right) \quad (\text{use P4}) \\ &= \mathcal{D}_{\omega_l^{[d]}} \mathbf{A}' \mathbf{A} \mathbf{x}. \quad (\text{use P6}) \end{aligned}$$

Concatenating (8) by columns leads to the matrix

$$\begin{aligned} & \begin{bmatrix} \frac{\partial \mathbf{A}'\mathbf{A}}{\partial \omega_1^{[d]}} & \cdots & \frac{\partial \mathbf{A}'\mathbf{A}}{\partial \omega_M^{[d]}} \end{bmatrix} \mathbf{x} \\ &= -\iota \mathbf{A}' \text{diag}\{\mathbf{A}(\mathbf{x} \odot \mathbf{r}^{[d]})\} \\ &+ \iota \text{diag}\{\mathbf{r}^{[d]}\} \mathbf{A}' \text{diag}\{\mathbf{A}\mathbf{x}\}. \end{aligned} \quad (9)$$

Alternatively, we can express the extended Jacobian as

$$\begin{aligned} & \begin{bmatrix} \frac{\partial \mathbf{A}'\mathbf{A}}{\partial \omega_1^{[d]}} & \cdots & \frac{\partial \mathbf{A}'\mathbf{A}}{\partial \omega_M^{[d]}} \end{bmatrix} \mathbf{x} \\ &= (\mathbf{x}^T \otimes \mathbf{I}_n) (\mathcal{D}_{\omega^{[d]}} \mathbf{A}'\mathbf{A}) \\ &= (\mathcal{D}_{\mathbf{A}'\mathbf{A}} \mathbf{A}'\mathbf{A}\mathbf{x}) (\mathcal{D}_{\omega^{[d]}} \mathbf{A}'\mathbf{A}) \\ &= \mathcal{D}_{\omega^{[d]}} \mathbf{A}'\mathbf{A}\mathbf{x}. \end{aligned} \quad (10)$$

Again we use NUFFT operations to approximate (10) efficiently.

F. Inverse of Positive Semidefinite (PSD) Operator

Image reconstruction methods based on algorithms like the augmented Lagrangian approach [33] use ‘‘data consistency’’ step that often involve least-squares problems having solutions of the following form [34], [35], [36]:

$$(\mathbf{A}'\mathbf{A} + \lambda \mathbf{I})^{-1} \mathbf{x},$$

for some vector $\mathbf{x} \in \mathbf{C}^N$, or

$$(\mathbf{A}'\mathbf{A} + \lambda \mathbf{T}'\mathbf{T})^{-1} \mathbf{x}, \quad (11)$$

where \mathbf{T} denotes a linear regularization operator that is independent of ω . In both cases, $\lambda > 0$ and the null spaces of \mathbf{T} and \mathbf{A} are disjoint, so the Hessian matrix is invertible. A few iterations of CG method usually suffices to efficiently compute the approximate product of such a matrix inverse with a vector. The direct inverse is impractical for large-scale problems like MRI. Following [35], we treat CG as solving the above equations accurately, so that we can derive efficient approximations as follows. Otherwise, attempting to auto-differentiate through a finite number of CG iterations would require undesirably large amounts of memory. Here we derive the corresponding Jacobian matrices for the exact inverse to (11) and then apply fast approximations. For \mathbf{x} , the Jacobian is

$$\begin{aligned} \frac{\partial (\mathbf{A}'\mathbf{A} + \lambda \mathbf{T}'\mathbf{T})^{-1} \mathbf{x}}{\partial \mathbf{x}} &= (\mathbf{A}'\mathbf{A} + \lambda \mathbf{T}'\mathbf{T})^{-1}, \\ \frac{\partial (\mathbf{A}'\mathbf{A} + \lambda \mathbf{T}'\mathbf{T})^{-1} \mathbf{x}}{\partial \mathbf{x}^*} &= 0. \end{aligned}$$

We can still use CG (with NUFFT) to efficiently multiply this Jacobian by a vector, albeit approximately.

To consider the Jacobian w.r.t. the sampling pattern $\omega^{[d]}$, define $\mathbf{z} = (\mathbf{A}'\mathbf{A} + \lambda \mathbf{T}'\mathbf{T})^{-1} \mathbf{x}$ and $\mathbf{F} = \mathbf{A}'\mathbf{A} + \lambda \mathbf{T}'\mathbf{T}$. We assume that \mathbf{A} and \mathbf{T} have disjoint null spaces, so that \mathbf{F}

is symmetric positive definite and hence invertible. Applying equalities derived above leads to the following Jacobian expression:

$$\begin{aligned} & \mathcal{D}_{\omega^{[d]}} \mathbf{F}^{-1} \mathbf{x} \\ &= (\mathcal{D}_{\mathbf{F}} \mathbf{F}^{-1} \mathbf{x}) (\mathcal{D}_{\omega^{[d]}} \mathbf{F}) \quad \text{use P6} \\ &= -(\mathbf{x}^T \otimes \mathbf{I}) ((\mathbf{F}^T)^{-1} \otimes \mathbf{F}^{-1}) (\mathcal{D}_{\omega^{[d]}} \mathbf{F}) \quad \text{use P5} \\ &= -((\mathbf{x}^T (\mathbf{F}^T)^{-1}) \otimes \mathbf{F}^{-1}) (\mathcal{D}_{\omega^{[d]}} \mathbf{F}) \quad \text{use P2} \\ &= -\mathbf{F}^{-1} (\mathbf{x}^T (\mathbf{F}^T)^{-1} \otimes \mathbf{I}) (\mathcal{D}_{\omega^{[d]}} \mathbf{F}) \quad \text{use P3} \\ &= -\mathbf{F}^{-1} (\mathcal{D}_{\omega^{[d]}} \mathbf{F} \mathbf{z}) \quad \text{use P4} \\ &= -(\mathbf{A}'\mathbf{A} + \lambda \mathbf{T}'\mathbf{T})^{-1} \left(-\iota \mathbf{A}' \text{diag}\{\mathbf{A}(\mathbf{z} \odot \mathbf{r}^{[d]})\} \right. \\ &\quad \left. + \iota \text{diag}\{\mathbf{r}^{[d]}\} \mathbf{A}' \text{diag}\{\mathbf{A}\mathbf{z}\} \right) \quad \text{use (10)}. \end{aligned} \quad (12)$$

We apply this Jacobian to a vector by using four NUFFT operations followed by running CG to approximate the product of \mathbf{F}^{-1} times a vector. Notably, the memory cost of (12) is constant w.r.t the number of iterations, whereas the standard auto-differentiation approach has linear memory cost. Using the proposed method, one may apply enough iterations to guarantee convergence. This new fast and low-memory Jacobian approximation is particularly important for enabling the MRI applications shown in the following sections. Without this approximation, memory requirements can be prohibitively large.

G. Sensitivity Maps

In multi-coil (parallel) acquisition, the MRI system model involves another linear operator

$$\mathbf{S} = \begin{bmatrix} \mathbf{S}_1 \\ \vdots \\ \mathbf{S}_{N_c} \end{bmatrix},$$

where $\mathbf{S}_i = \text{diag}\{s_i\}$ denotes a diagonal matrix containing the receiver coil sensitivity map [26]. The total number of receiver channels is N_c . The system matrix (\mathbf{E}) for MRI in this case becomes $(\mathbf{I}_{N_c} \otimes \mathbf{A})\mathbf{S}$. Because of the special block-diagonal structure of \mathbf{S} , all the Jacobian matrices in previous sections still hold by simply replacing \mathbf{A} with \mathbf{E} .

The Jacobian derivations are as follows. For the forward operator (II-C), one can show

$$\begin{aligned} \frac{\partial \mathbf{E}\mathbf{x}}{\partial \omega^{[d]}} &= \frac{\partial \begin{bmatrix} \mathbf{A}\mathbf{S}_1\mathbf{x} \\ \vdots \\ \mathbf{A}\mathbf{S}_{N_c}\mathbf{x} \end{bmatrix}}{\partial \omega^{[d]}} \\ &= \begin{bmatrix} -\iota \text{diag}\{\mathbf{A}(s_1 \odot \mathbf{x} \odot \mathbf{r}^{[d]})\} \\ \vdots \\ -\iota \text{diag}\{\mathbf{A}(s_{N_c} \odot \mathbf{x} \odot \mathbf{r}^{[d]})\} \end{bmatrix} \\ &= \iota \text{diag}\left\{ (\mathbf{I}_{N_c} \otimes \mathbf{A}) \mathbf{S}(\mathbf{x} \odot \mathbf{r}^{[d]}) \right\} \\ &= \iota \text{diag}\left\{ \mathbf{E}(\mathbf{x} \odot \mathbf{r}^{[d]}) \right\}. \end{aligned}$$

The adjoint operator (II-D) follows the same proof and produces

$$\frac{\partial \mathbf{E}' \mathbf{y}}{\partial \boldsymbol{\omega}^{[d]}} = \iota \text{diag}\{\mathbf{r}^{[d]}\} \mathbf{E}' \text{diag}\{\mathbf{y}\}.$$

For the gram operator (II-E) we have

$$\begin{aligned} \frac{\partial \mathbf{E}' \mathbf{E} \mathbf{x}}{\partial \boldsymbol{\omega}^{[d]}} &= \sum_i \frac{\partial \mathbf{S}'_i \mathbf{A}' \mathbf{A} \mathbf{S}_i \mathbf{x}}{\partial \boldsymbol{\omega}^{[d]}} \\ &= \sum_i \mathbf{S}'_i \frac{\partial \mathbf{A}' \mathbf{A} \mathbf{S}_i \mathbf{x}}{\partial \boldsymbol{\omega}^{[d]}} \\ &= \sum_i -\iota \mathbf{S}'_i \mathbf{A}' \text{diag}\{\mathbf{A}(\mathbf{S} \mathbf{x} \odot \mathbf{r}^{[d]})\} \\ &\quad + \iota \mathbf{S}'_i \text{diag}\{\mathbf{r}^{[d]}\} \mathbf{A}' \text{diag}\{\mathbf{A} \mathbf{S}_i \mathbf{x}\} \\ &= \sum_i -\iota \mathbf{S}'_i \mathbf{A}' \text{diag}\{\mathbf{A}(\mathbf{S} \mathbf{x} \odot \mathbf{r}^{[d]})\} \\ &\quad + \iota \text{diag}\{\mathbf{r}^{[d]}\} \mathbf{S}'_i \mathbf{A}' \text{diag}\{\mathbf{A} \mathbf{S}_i \mathbf{x}\} \\ &= -\iota \mathbf{E}' \text{diag}\{\mathbf{E}(\mathbf{x} \odot \mathbf{r}^{[d]})\} \\ &\quad + \iota \text{diag}\{\mathbf{r}^{[d]}\} \mathbf{E}' \text{diag}\{\mathbf{E} \mathbf{x}\}. \end{aligned} \quad (13)$$

For the inverse of PSD (II-F), let $\mathbf{G} = \mathbf{E}' \mathbf{E} + \lambda \mathbf{T}' \mathbf{T}$ and $\mathbf{z} = \mathbf{G}^{-1} \mathbf{x}$ (in the usual case where the regularizer matrix \mathbf{T} is designed such that \mathbf{G} is invertible). Combining (12) and (13) produces :

$$\begin{aligned} &\frac{\partial (\mathbf{E}' \mathbf{E} + \lambda \mathbf{T}' \mathbf{T})^{-1} \mathbf{x}}{\partial \boldsymbol{\omega}^{[d]}} \\ &= -\mathbf{G}^{-1} (\mathbf{x}^T (\mathbf{G}^T)^{-1} \otimes \mathbf{I}) \mathcal{D}_{\boldsymbol{\omega}^{[d]}} \mathbf{G} \\ &= -(\mathbf{E}' \mathbf{E} + \lambda \mathbf{T}' \mathbf{T})^{-1} \left(-\iota \mathbf{E}' \text{diag}\{\mathbf{E}(\mathbf{z} \odot \mathbf{r}^{[d]})\} \right. \\ &\quad \left. + \iota \text{diag}\{\mathbf{r}^{[d]}\} \mathbf{E}' \text{diag}\{\mathbf{E} \mathbf{z}\} \right). \end{aligned}$$

Again, we apply this Jacobian matrix to a vector by combining NUFFTs and CG.

H. Field Inhomogeneity

For MRI scans with long readouts, one should also consider the effects of off-resonance (e.g., \mathbf{B}_0 field inhomogeneity), in which case the system matrix elements are given by [5]

$$a_{ij} = e^{-i\bar{\omega}_i \cdot \bar{r}_j} e^{-i w_j t_i},$$

where w_j denotes the field map value at the j th voxel and t_i is the time of the i th readout sample.

This form is no longer a Fourier transform operation, but there are fast and accurate approximations [37] that enable the use of $O(N \log N)$ NUFFT steps and avoid the very slow $O(N^2)$ matrix-vector multiplication that would be needed otherwise. Such approximations of system matrix \mathbf{E} usually have the form:

$$\mathbf{E}_f \approx \sum_{l=1}^L \text{diag}\{b_{il}\} \mathbf{A}(\boldsymbol{\omega}) \text{diag}\{c_{lj}\},$$

where \mathbf{A} denotes the usual (possibly non-uniform) DFT that is usually approximated by a NUFFT, $b_{il} \in \mathbb{C}^M$, and $c_{lj} \in \mathbb{C}^N$. It

is relatively straightforward to generalize the Jacobian expressions in this paper to handle the case of field inhomogeneity, by simply replacing \mathbf{A} with \mathbf{E}_f , similar to the sensitivity map case.

III. OPTIMIZE SAMPLING PATTERNS

For modern MRI systems, the sampling trajectory $\boldsymbol{\omega}$ is a programmable parameter. Traditionally $\boldsymbol{\omega}$ is a geometrical curve controlled by few parameters (such as radial spokes or spiral leaves), and its tuning relies on derivative-free optimization such as grid-search. In this paper, we optimize $\boldsymbol{\omega}$ by minimizing a training loss function from image reconstruction, where the descent direction of $\boldsymbol{\omega}$ is the negative gradient of that loss [19], [21]. We adopted such ‘‘reconstruction loss’’ because the ultimate goal of sampling pattern optimization is to improve image quality. To learn from large datasets, $\boldsymbol{\omega}$ is optimized using stochastic gradient descent (SGD)-like algorithms. Additionally, the loss function can contain other terms, such as a penalty on the maximum gradient strength and slew rate [19], [21].

For image reconstruction, consider a convex and smooth regularizer $\mathbf{R}(\cdot)$ for simplicity. Since the noise statistics are Gaussian, a typical regularized cost function used for model-based image reconstruction is [5]

$$\Psi(\mathbf{x}) = \frac{1}{2} \|\mathbf{A} \mathbf{x} - \mathbf{y}\|_2^2 + \mathbf{R}(\mathbf{x}). \quad (14)$$

For illustration, consider applying the k th step of gradient descent (GD) to that cost function:

$$\begin{aligned} \mathbf{x}_{k+1} &= \mathbf{x}_k - \alpha \nabla \Psi(\mathbf{x}_k) \\ &= \mathbf{x}_k - \alpha \mathbf{A}(\boldsymbol{\omega})' (\mathbf{A}(\boldsymbol{\omega}) \mathbf{x}_k - \mathbf{y}) - \alpha \nabla \mathbf{R}(\mathbf{x}_k), \end{aligned}$$

where $\mathbf{x}_k \in \mathbb{C}^N$, α is a step size, and \mathbf{A}' denotes the Hermitian transpose of \mathbf{A} . After running K iterations, we have a reconstructed image (batch) $\mathbf{x}_K = \mathbf{x}_K(\boldsymbol{\omega}) = f(\boldsymbol{\omega}, \mathbf{y})$, where the reconstruction method $f(\boldsymbol{\omega}, \mathbf{y})$ is a function of both the data \mathbf{y} and the sampling pattern $\boldsymbol{\omega}$. To learn/update the sampling pattern $\boldsymbol{\omega}$, consider the loss function for a single training example:

$$L(\boldsymbol{\omega}) = \|\mathbf{x}_K(\boldsymbol{\omega}) - \mathbf{x}^{\text{true}}\|_2^2 \quad (15)$$

where $L: \mathbb{R}^M \mapsto \mathbb{R}$ and \mathbf{x}^{true} is the reference fully-sampled image (batch). Learning $\boldsymbol{\omega}$ via backpropagation (or chain-rule) requires differentiating L w.r.t. the sampling pattern $\boldsymbol{\omega}$, which in turn involves Jacobians of quantities like $\mathbf{A}(\boldsymbol{\omega})$ that we derived above.

During training, the observation \mathbf{y} can be retrospectively simulated:

$$\mathbf{y} = \mathbf{A}(\boldsymbol{\omega}) \mathbf{x}^{\text{true}}.$$

Although we illustrate the GD algorithm with a simple smooth regularizer, more generally, the reconstruction method $f(\boldsymbol{\omega}, \mathbf{y})$ can involve more sophisticated regularizers such as neural networks [19], [21] or non-smooth sparsity models [38] used in compressed sensing. In such cases, subgradients, instead of gradients, are adopted during the backpropagation, as commonly used in stochastic optimization. The loss is still

backpropagated through iterative steps to compute a gradient w.r.t. ω .

The loss function L is a real-valued scalar function, hence non-holomorphic [30], whereas the image \mathbf{x} and other intermediate variables are complex-valued. In this situation, the gradient descent step can update the real and imaginary part of separately and still use Wirtinger derivatives. For example, suppose $z = a + ni$, $a, b \in \mathbb{R}$,

$$z_{n+1} = z_n - \alpha/2 * \frac{\partial L}{\partial a} - i\alpha/2 * \frac{\partial L}{\partial b} = z_n - \alpha * \frac{\partial L}{\partial z^*},$$

where L is the loss function and α is the step size. See [30] for the derivation.

Suppose $s = f(z)$ And the chain rule in backpropagation becomes [30]:

$$\frac{\partial L}{\partial z^*} = \left(\frac{\partial L}{\partial s^*}\right)^* \frac{\partial s}{\partial z^*} + \frac{\partial L}{\partial s^*} \left(\frac{\partial s}{\partial z}\right)^*.$$

Here we use the forward operator (II-C) as an example of backpropagation. As needed in a backpropagation step (Jacobian-vector product, JVP), one needs to apply the Jacobian (4) to a gradient vector $\mathbf{v} = \frac{\partial L}{\partial (\mathbf{A}\mathbf{x})^*} \in \mathbb{C}^M$. The corresponding vector is

$$\frac{\partial L}{\partial \omega} = \text{real}\left\{(-i \mathbf{A}(\mathbf{x} \odot \mathbf{r}^{[d]})' \odot \mathbf{v})\right\}. \quad (16)$$

To compute this term efficiently, we simply apply a NUFFT operation to $\mathbf{x} \odot \mathbf{r}^{[d]}$, followed by a point-wise multiplication with \mathbf{v} . The Gram and PSD inverse (“data consistency”) term in II-E and II-F follow a similar manner during backpropagation. See our open-source codes ² for implementation details.

Furthermore, learning-based approaches are very compute-intensive during end-to-end training, especially for the 3D cases. Therefore, it is desirable to accelerate computation by using faster NUFFT approximations (low over-sampling factors and/or small interpolation neighborhoods) in the early epochs of training. Later, when the method is deployed on test data or prospectively acquired data, one could use higher NUFFT accuracy.

Note that the proposed approach is applicable only to non-Cartesian MRI, because Cartesian sampling pattern design is usually a discrete optimization problem, incompatible with gradient-based methods. However, one could optimize phase-encode locations continuously (in 2D or 3D) with the frequency-encoding direction being fully sampled, which is a hybrid Cartesian / non-Cartesian approach [20].

IV. EXPERIMENTS

This section validates the accuracy and efficiency of the proposed methods. It also showcases the application to MRI sampling trajectory optimization.

A. Accuracy and Efficiency

We implemented the numerical experiments with torchkbnufft³ [39] and MIRTorch⁴ toolboxes.

²<https://github.com/guanhuaw/Bjork>

³<https://github.com/mmuckley/torchkbnufft>

⁴<https://github.com/guanhuaw/MIRTorch>

We first considered the following test cases

$$\frac{\partial \|f(\mathbf{x})\|_2^2}{\partial \omega^{[d]}} \quad \text{and} \quad \frac{\partial \|f(\mathbf{x})\|_2^2}{\partial \mathbf{x}^*},$$

where $f(\cdot)$ stands for a forward, Gram, or ‘inverse of PSD’ (II-F) of sensitivity-informed NUFFTs (II-G). The Gram and inverse experiments implicitly test the adjoint operator’s approximations. The \mathbf{x} adopted is a 40×40 patch cropped from the center of a Shepp–Logan phantom with random additional phases (uniformly distributed in $[-\pi, \pi]$). \mathbf{S} is a simulated 8-channel sensitivity map, and ω is one radial spoke crossing the k-space center. The Jacobian calculation methods are: (1) auto-differentiation of NUFFT; the lookup table operation [24] is replaced by bilinear interpolation to enable auto-differentiation, as adopted by [19], (2) our approximation described above, (3) auto-differentiation of exact non-uniform discrete Fourier transform (NUDFT), implemented with single precision. We regard method 3 (NUDFT) as the ground truth. Since NUDFT (in its simplest form) only involves one exponential function, multiplication and addition for each element, its backpropagation introduces minimal numerical errors. For the inverse of PSD, we applied 20 CG iterations for all three methods, which is adequate for convergence based on the residual value.

Fig. 1 and Fig. 2 illustrate representative profiles of the gradients w.r.t. \mathbf{x} and ω . For ω , the auto-differentiation (method 1) approach has larger deviations from method 3 (NUDFT) because of the non-differentiability of interpolation operations w.r.t. coordinates. For the gradient w.r.t. \mathbf{x} , both method 1 and method 2 generate accurate results for forward and Gram operators. The reason is that in method 1 (auto-diff), the interpolation operation w.r.t. \mathbf{x} is linear, hence accurately differentiable. For the inverse (of PSD) operator, method 1 leads to a slightly inaccurate gradient, stemming from the accumulated errors of backpropagating CG iterations. The center of trajectories optimized with quadratic regularizers (CG-SENSE and QPLS) is not aligned with the k-space center. We hypothesize that regularizers (and corresponding iterative algorithms) handle image phases differently, leading to distinct trajectory centers.

Table I and Table II compare the time and memory cost of methods 1 (auto-diff) and 2 (proposed). The CPU is Intel(R) Xeon(R) Gold 6138 CPU @ 2.00GHz and the GPU is an Nvidia(R) RTX2080Ti. We used PyTorch 1.9.1 and torchkbnufft 1.1.0. The memory usage is tracked by `torch.cuda.memory_allocated` on Nvidia GPUs.

Our method is much faster than auto-differentiation on both GPUs and CPUs, and uses much less memory. Importantly, the PSD inverse Jacobian was impossible for the 3D case, whereas the proposed approach fit comfortably in GPU memory.

B. MRI Trajectory Optimization

This experiment optimized the MRI sampling trajectory using the proposed Jacobian approximations and stochastic optimization. The reconstruction methods (14) here include two types of algorithms, namely smooth (regularized) least-squares reconstruction and sparsity-based reconstruction.

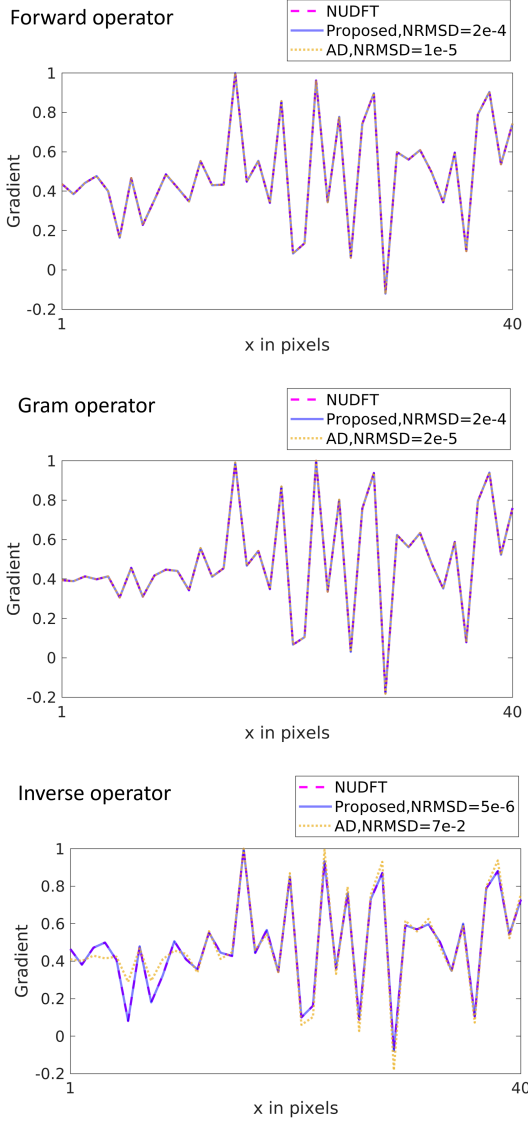


Fig. 1. Examples of gradients w.r.t. \mathbf{x}^* (the real part is plotted). Plots show one representative row of a 40×40 matrix (rescaled to $[-1,1]$). The rows are the forward, Gram, and ‘inverse of PSD’ operator cases. Three calculation methods (in three columns) achieve very similar results. The horizontal axis is the pixel index. The bottom left corner of each plot shows the normalized root-mean-square difference (NRMSD) compared with the reference NUDFT calculation.

TABLE I
COMPUTATION TIME OF THE TEST CASE.

	Gram		Inverse	
	auto-diff	proposed	auto-diff	proposed
Large image - GPU	0.3s	0.2s	4.3s	2.5s
Small image - GPU	0.1s	0.1s	1.3s	0.9s
Large image - CPU	5.2s	1.7s	276.2s	48.5s
Small image - CPU	0.8s	0.5s	27.4s	6.9s

Large size: 400×400 ; small size: 40×40

20 CG iterations were applied in the PSD inverse cases.

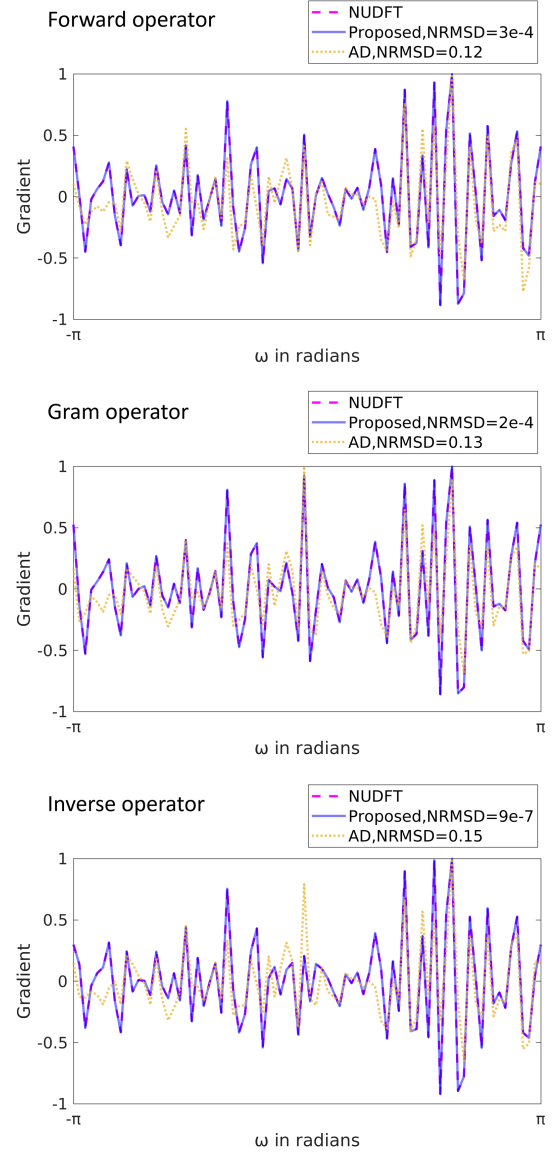


Fig. 2. Examples of gradients w.r.t. ω . Plots show one spoke of 80 points (rescaled to $[-1,1]$). The rows are the forward, Gram, and ‘inverse of PSD’ operator cases. The proposed approximation better matches the gradient of the NUDFT. The bottom left corner of each plot shows the normalized root-mean-square difference (NRMSD) compared with the NUDFT calculation.

TABLE II
MEMORY USE OF THE TEST CASE.

	Gram		Inverse	
	standard	proposed	standard	proposed
Small image	3.1MB	2.8MB	145.7MB	2.9MB
Large image	375.9MB	267.5MB	5673.2MB	272.0MB
3D volume	N/A	10.1GB	N/A	10.8GB

Large size: 400×400 ; small size: 40×40 ; 3D volume: $200 \times 200 \times 100$.

N/A: the memory use is too large for a single GPU.

20 CG iterations were applied in the PSD inverse cases.

The smooth reconstruction method uses the cost function

$$\Psi(\mathbf{x}) = \frac{1}{2}\|\mathbf{E}(\boldsymbol{\omega})\mathbf{x} - \mathbf{y}\|_2^2 + \frac{\lambda}{2}\|\mathbf{T}\mathbf{x}\|_2^2,$$

where \mathbf{T} is a finite-difference operator encouraging smoothness. Correspondingly, the reconstructed image is:

$$\mathbf{x}_K = (\mathbf{E}'\mathbf{E} + \lambda\mathbf{T}'\mathbf{T})^{-1}\mathbf{E}'\mathbf{y},$$

which we used CG to solve. The following sections refer to this method as quadratic penalized least-squares (QPLS). We also implemented a simpler case, where $\mathbf{T} = \mathbf{I}$, which is referred as CG-SENSE [40]. In both scenarios, we set λ to 10^{-3} empirically and applied 20 CG iterations. The initialization of CG used the density compensated reconstruction [41]. The number of iterations was determined based on the residual norm $\|\mathbf{A}\hat{\mathbf{x}} - \mathbf{y}\|/\|\mathbf{y}\|$.

The sparsity-based compressed (CS) sensing algorithm here adopts a wavelets-based sparsity penalty, and has the following objective function

$$\Psi(\mathbf{x}) = \frac{1}{2}\|\mathbf{E}(\boldsymbol{\omega})\mathbf{x} - \mathbf{y}\|_2^2 + \lambda\|\mathbf{W}\mathbf{x}\|_1,$$

where \mathbf{W} is an orthogonal DWT matrix and we set $\lambda = 10^{-5}$ empirically. We used 40 iterations of the proximal optimized gradient method (POGM) [42], [43] to solve this non-smooth optimization problem.

For the purpose of comparing trajectories and image quality, we also applied the proposed approximations to reconstruction using an unrolled neural network (UNN) that followed the definition of [35] ([21] extends it to non-Cartesian cases.) We used the same network configuration as in [21].

To optimize the k-space trajectory for each of these reconstruction methods, the training loss (15) is:

$$L(\boldsymbol{\omega}) = \|\mathbf{x}_K(\boldsymbol{\omega}) - \mathbf{x}^{\text{true}}\|_2^2 + \mu_1\phi_{\gamma\Delta t g_{\max}}(|\mathbf{D}_1\boldsymbol{\omega}|) + \mu_2\phi_{\gamma\Delta t^2 s_{\max}}(|\mathbf{D}_2\boldsymbol{\omega}|),$$

where \mathbf{x}^{true} is the conjugate phase reconstruction of fully sampled Cartesian data [44]. The second and third terms apply a soft constraint on gradient strength and slew rate according to [21, Eqn. 2], where $\phi_\lambda(|\mathbf{x}|) = \sum \max(|\mathbf{x}| - \lambda, 0)$. The maximum gradient strength (g_{\max}) is 5 Gauss/cm and the maximum slew rate (s_{\max}) is 15 Gauss/cm/ms. $\mu_1 = \mu_2 = 10$. We estimated sensitivity maps in \mathbf{E} using ESPIrIT [45], and simulated raw signal $\mathbf{y} = \mathbf{E}(\boldsymbol{\omega})\mathbf{x}^{\text{true}}$ retrospectively w.r.t. candidate trajectories. The training uses the fastMRI brain dataset [46] containing 15902 T1w slices, 16020 T2w slices, and 3311 FLAIR slices cropped to size 320×320 . The number of coils ranges from 2 to 28. We used the Adam optimizer [47], with step size 10^{-4} and mini-batch size 12. We used 6 epochs for training model-based methods (CG-SENSE, QPLS and CS) and 60 epochs for the UNN training. The initialization of learned trajectories is an under-sampled radial trajectory in all experiments. The initialization has 16 ‘‘spokes’’ and each spoke is 5ms long with 1280 sampling points. We also adopted the k-space parameterization trick detailed in [21, Eqn. 3] to avoid sub-optimal local minima. We parameterized each shot with 40 quadratic spline kernels.

Fig. 3 showcases the trajectories optimized for each of the reconstruction methods. The sparsity regularizer prompts very

different sampling trajectories than the quadratic regularizer, especially in the central k-space.

Table III shows the average image reconstruction quality (PSNR and SSIM [48], fully sampled image as the ground truth) on 500 test slices. It also showcases the image quality of these learned trajectories with reconstruction methods different from the training phase. All learned trajectories lead to improved reconstruction quality compared to the initial radial trajectory, even with different reconstruction methods. Importantly, the same reconstruction algorithm across training and test lead to the greatest improvement (the bold diagonal entries). Fig. 4 shows reconstruction examples.

TABLE III
AVERAGE RECONSTRUCTION QUALITY ON TEST SET WITH TRAJECTORIES LEARNED FOR DIFFERENT RECONSTRUCTION METHODS.

SSIM						
Test	Learn	QPLS	CG-SENSE	CS	UNN	unoptimized
	QPLS	0.963	0.963	0.962	0.961	0.947
CG-SENSE	0.964	0.964	0.963	0.961	0.946	
CS	0.962	0.963	0.966	0.964	0.946	
UNN	0.960	0.960	0.958	0.964	0.950	

PSNR (in dB)						
Test	Learn	QPLS	CG-SENSE	CS	UNN	unoptimized
	QPLS	35.1	35.1	34.9	35.0	33.1
CG-SENSE	35.2	35.2	34.9	35.1	33.1	
CS	34.8	34.9	35.4	35.2	33.0	
UNN	34.6	34.6	34.5	35.0	33.5	

Learn: the reconstruction method that the trajectory is trained with.

Test: the reconstruction method in the test phase.

unoptimized: the undersampled radial trajectory (initialization).

C. Accelerated Learning with Low-Accuracy NUFFT

The major computation cost of trajectory learning is with NUFFTs and their Jacobian calculations. To accelerate the training, we propose an empirical approach: using NUFFTs with a smaller gridding size and interpolation kernel size during training [25], and still using standard (slower) NUFFTs during inference. Here we investigated learning trajectories with two different NUFFT accuracies: (1) gridding size = $1.25 \times$ image size, interpolation kernel size = 5 and (2) gridding size = $2 \times$ image size, interpolation kernel size = 6 which is a commonly used setting. On our GPUs, the lower-accuracy setting is $1.4 \times$ faster than the higher-accuracy one. We use the CS-based reconstruction and corresponding training strategy described in the previous subsection. Fig. 5 shows the trajectory optimized by two NUFFT accuracy levels. To compare the trajectory optimized by these two settings, we used the terminal task, the reconstruction image quality, as the evaluation metric. We simulated and reconstructed images using the two trajectories on the test data (500 slices in the previous experiment). The trajectories optimized with the ‘‘low accuracy’’ and ‘‘high accuracy’’ NUFFT led to mean PSNR values of 35.4 ± 4.6 dB and 35.4 ± 4.7 dB.

V. DISCUSSION

This paper presents a model-based approximation of Jacobian matrices involving NUFFTs. Compared to direct auto-

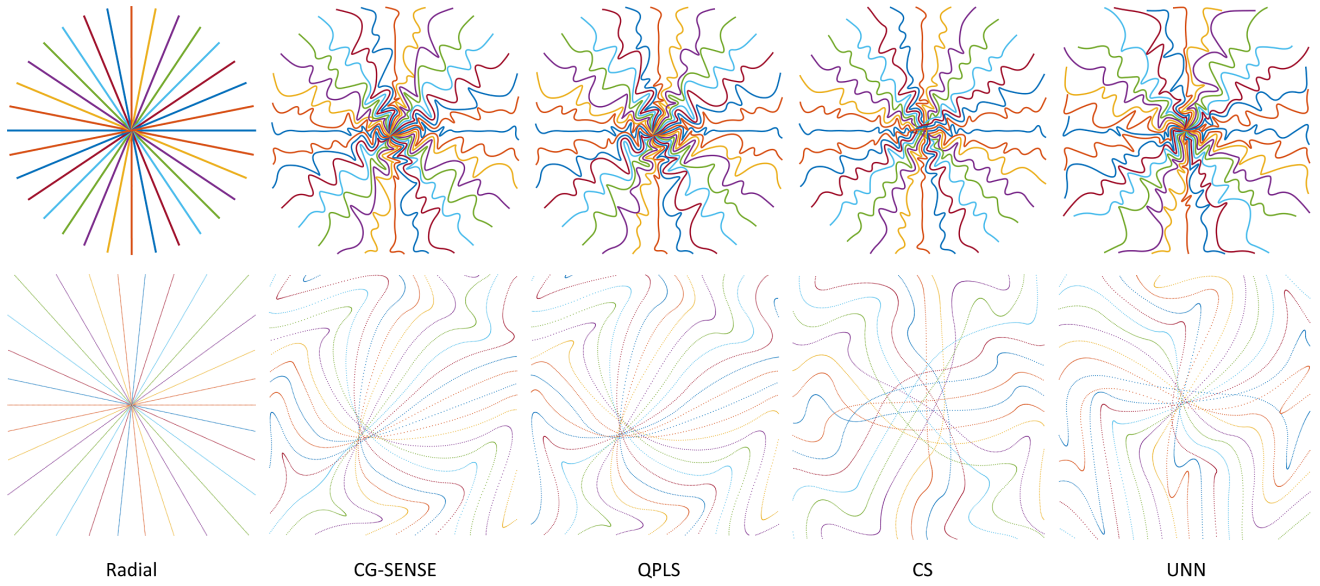


Fig. 3. Optimized sampling trajectories for several iterative reconstruction methods. The left column shows the uniform radial initialization. The second row shows the $8\times$ zoomed-in central k-space.

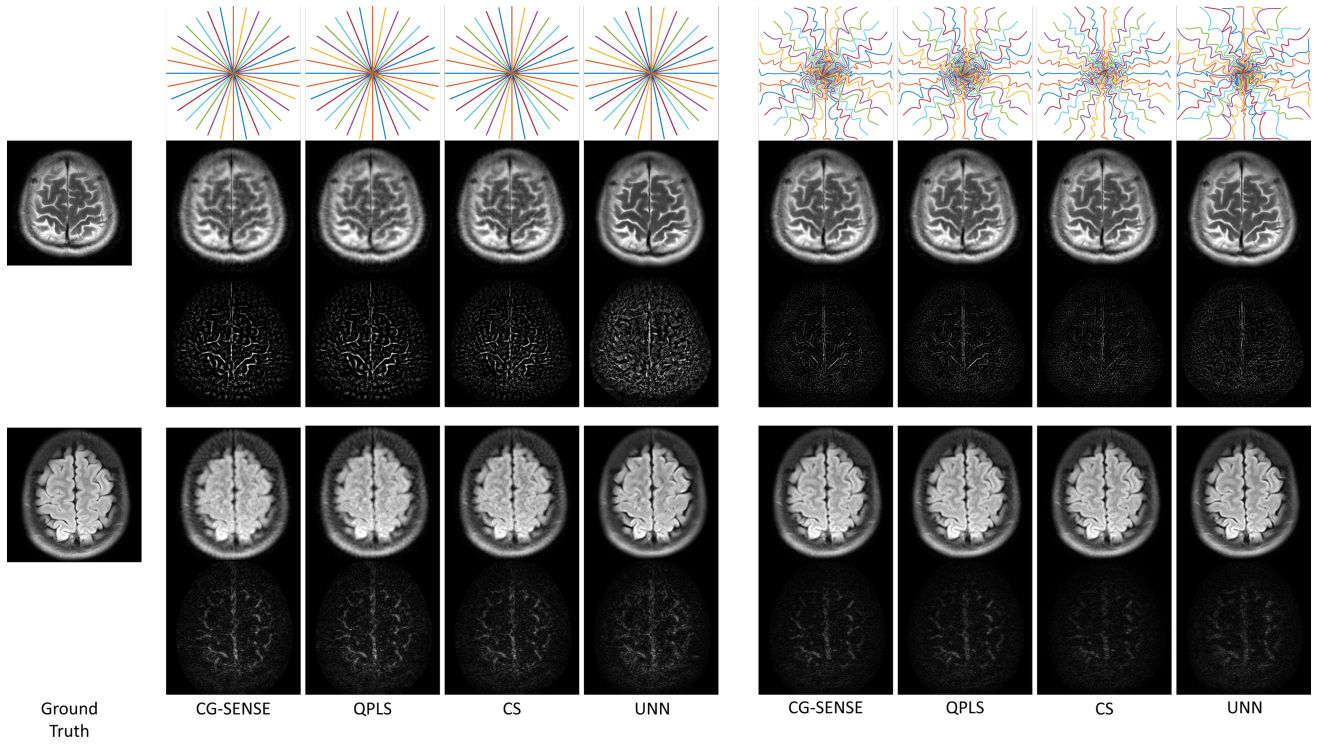


Fig. 4. Examples of the reconstructed images with unoptimized (left) and optimized trajectories (right). The third row shows corresponding error maps.

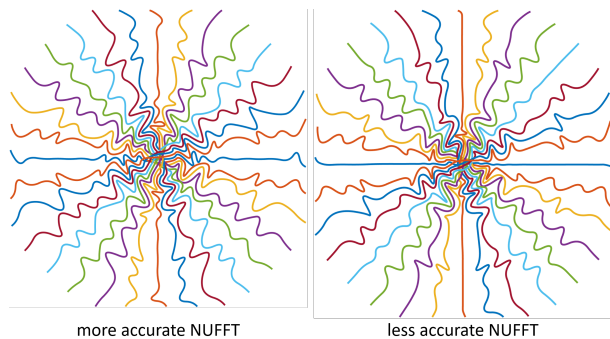


Fig. 5. Learned trajectories with different NUFFT accuracies.

differentiation (AD), the proposed method is faster, uses less memory, and better approximates the reference NUFFT results. As discussed in II-B, the deviation of AD is not a software limitation, but rather a problem that stems from the non-differentiability of interpolation or lookup table. NUFFT alternatives such as re-gridding or filtered back-projection also suffer from similar non-differentiability issues and are less effective than iterative reconstruction. Our previous studies [21, Fig. 14] compared the trajectory optimization results of the proposed method and standard AD. The trajectory optimized by the proposed approximation led to better image quality, and conformed better to the empirical criteria [49], [50]: sampling points should not be overlapped with or too distant from each other. [21] also tested the optimized trajectory in a prospective in-vivo experiment, and discussed practical issues, including eddy currents and the mismatch between training set and prospective protocols.

To accelerate training, one may use crude NUFFT approximations in the early epochs and switch to accurate approximations in later epochs or during deployment. It is also preferable to precalculate the Toeplitz embedding kernel [37], [51] to further accelerate iterative reconstruction.

We showcased an application of the proposed approach with MRI experiments where the frequency domain sampling strategy is learned w.r.t. user-defined reconstruction methods. This optimization-based approach exploits the synergy between sampling and reconstruction, and learns effective sampling strategies from training data. These topics can be investigated for other computational imaging modalities. Several previous studies [19], [21] only used NN-based reconstruction methods. The stability and generalizability of NN-based reconstruction is still under investigation. In comparison, by using our method delineated in III, one may optimize trajectory for model-based reconstruction methods that may be more robust and interpretable. Our results show that with a suitably tailored sampling pattern, traditional model-based reconstruction can compete with NN-based reconstruction, reinforcing related observations in recent work [52]. Importantly, sampling optimization for model-based reconstruction requires much less training data than for NN-based reconstruction. This property is beneficial for medical imaging where data availability is often limited.

The training used discrete-space image datasets, whereas

the actual objects in practice are continuous. Ideally, using the accurate continuous image model could better approximate the actual situation. This implicit bias is common for learning-based methods. Subsequent investigations may use analytical phantoms and compare optimized trajectories using discrete-space and continuous-space models.

Sampling patterns learned with different reconstruction methods show distinct characteristics. This phenomenon is also observed in previous literature [15], [17]. The differences in sampling patterns may stem from different regularizers, as well as different iterative algorithms. Also, as shown in III, the synergistic sampling and reconstruction leads to the best image quality. Interestingly, for the standard radial trajectory, the UNN approach outperformed the CS approach; but after trajectory optimization, the CS approach had higher SNR than the UNN approach. Such evidence further supports the advantage of joint optimization of sampling and reconstruction.

ACKNOWLEDGMENT

The authors gratefully thank Dr. Douglas Noll, Dr. Tianrui Luo, and Naveen Murthy for helpful advice.

REFERENCES

- [1] D. C. Munson and J. L. Sanz, "Image reconstruction from frequency-offset Fourier data," *Proc. IEEE*, vol. 72, no. 6, pp. 661–9, Jun. 1984.
- [2] M. M. Bronstein, A. M. Bronstein, M. Zibulevsky, and H. Azhari, "Reconstruction in diffraction ultrasound tomography using nonuniform FFT," *IEEE Trans. Med. Imag.*, vol. 21, no. 11, pp. 1395–1401, Nov. 2002.
- [3] S. Matej, J. A. Fessler, and I. G. Kazantsev, "Iterative tomographic image reconstruction using Fourier-based forward and back-projectors," *IEEE Trans. Med. Imag.*, vol. 23, no. 4, pp. 401–12, Apr. 2004.
- [4] K. L. Wright, J. I. Hamilton, M. A. Griswold, V. Gulani, and N. Seiberlich, "Non-Cartesian parallel imaging reconstruction," *J. Magn. Reson. Imag.*, vol. 40, no. 5, pp. 1022–1040, 2014.
- [5] J. A. Fessler, "Model-based image reconstruction for MRI," *IEEE Sig. Proc. Mag.*, vol. 27, no. 4, pp. 81–9, Jul. 2010.
- [6] J. A. Fessler and B. P. Sutton, "Nonuniform fast Fourier transforms using min-fmax interpolation," *IEEE Trans. Sig. Proc.*, vol. 51, no. 2, pp. 560–74, Feb. 2003.
- [7] Z. Yang and M. Jacob, "Mean square optimal NUFFT approximation for efficient non-Cartesian MRI reconstruction," *J. Mag. Res.*, vol. 242, pp. 126–35, May 2014.
- [8] Y. Cao and D. N. Levin, "Feature-recognizing MRI," *Magn. Reson. Med.*, vol. 30, no. 3, pp. 305–317, 1993.
- [9] Y. Gao and S. Reeves, "Optimal k-space sampling in MRSI for images with a limited region of support," *IEEE Trans. Med. Imag.*, vol. 19, no. 12, pp. 1168–1178, Dec. 2000.
- [10] D. Xu, M. Jacob, and Z. Liang, "Optimal sampling of k-space with cartesian grids for parallel MR imaging," in *Proc. Intl. Soc. Mag. Res. Med.*, 2005, p. 2450.
- [11] M. Seeger, H. Nickisch, R. Pohmann, and B. Schölkopf, "Optimization of k-space trajectories for compressed sensing by Bayesian experimental design," *Magn. Reson. Med.*, vol. 63, no. 1, pp. 116–126, 2010.
- [12] J. P. Haldar and D. Kim, "OEDIPUS: An Experiment Design Framework for Sparsity-Constrained MRI," *IEEE Trans. Med. Imaging*, vol. 38, no. 7, pp. 1545–1558, Jul. 2019.
- [13] C. D. Bahadir, A. Q. Wang, A. V. Dalca, and M. R. Sabuncu, "Deep-learning-based optimization of the under-sampling pattern in MRI," *IEEE Trans. Comput. Imag.*, vol. 6, pp. 1139–1152, 2020.
- [14] F. Knoll, C. Clason, C. Diwok, and R. Stollberger, "Adapted random sampling patterns for accelerated MRI," *Mag. Res. Mat. Phys. Bio. Med.*, vol. 24, no. 1, pp. 43–50, Feb. 2011.
- [15] B. Gözcü, T. Sanchez, and V. Cevher, "Rethinking Sampling in Parallel MRI: A Data-Driven Approach," in *2019 27th Euro. Sig. Proc. Conf. (EUSIPCO)*, Sep. 2019, pp. 1–5.

- [16] I. A. M. Huijben, B. S. Veeling, and R. J. G. van Sloun, "Learning sampling and model-based signal recovery for compressed sensing MRI," in *2020 IEEE Intl. Conf. on Acous., Speech and Sig. Proc. (ICASSP)*, May 2020, pp. 8906–8910.
- [17] M. V. W. Zibetti, G. T. Herman, and R. R. Regatte, "Fast data-driven learning of parallel MRI sampling patterns for large scale problems," *Sci Rep.*, vol. 11, no. 1, p. 19312, Sep. 2021.
- [18] F. Sherry, M. Benning, J. C. D. Reyes, M. J. Graves, G. Maierhofer, G. Williams, C.-B. Schonlieb, and M. J. Ehrhardt, "Learning the sampling pattern for MRI," *IEEE Trans. Med. Imag.*, vol. 39, no. 12, pp. 4310–21, Dec. 2020.
- [19] T. Weiss, O. Senouf, S. Vedula, O. Michailovich, M. Zibulevsky, and A. Bronstein, "PILoT: Physics-informed learned optimized trajectories for accelerated MRI," *MELBA*, pp. 1–23, 2021.
- [20] H. K. Aggarwal and M. Jacob, "J-MoDL: Joint model-based deep learning for optimized sampling and reconstruction," *IEEE J. Sel. Top. Sig. Proc.*, vol. 14, no. 6, pp. 1151–62, Oct. 2020.
- [21] G. Wang, T. Luo, J.-F. Nielsen, D. C. Noll, and J. A. Fessler, "B-Spline Parameterized Joint Optimization of Reconstruction and K-Space Trajectories (BJORK) for Accelerated 2D MRI," *IEEE Trans. Med. Imag.*, vol. 41, no. 9, pp. 2318–2330, Sep. 2022.
- [22] S. P. Jordan, S. Hu, I. Rozada, D. F. McGivney, R. Boyaciouglu, D. C. Jacob, S. Huang, M. Beverland, H. G. Katzgraber, M. Troyer *et al.*, "Automated design of pulse sequences for magnetic resonance fingerprinting using physics-inspired optimization," *Proc. Natl. Acad. Sci.*, vol. 118, no. 40, p. e2020516118, 2021.
- [23] E. Scope Crafts, H. Lu, H. Ye, L. L. Wald, and B. Zhao, "An efficient approach to optimal experimental design for magnetic resonance fingerprinting with B-splines," *Magn. Reson. Med.*, vol. 88, no. 1, pp. 239–253, 2022.
- [24] B. Dale, M. Wendt, and J. L. Duerk, "A rapid look-up table method for reconstructing MR images from arbitrary K-space trajectories," *IEEE Trans. Med. Imag.*, vol. 20, no. 3, pp. 207–17, Mar. 2001.
- [25] P. J. Beatty, D. G. Nishimura, and J. M. Pauly, "Rapid gridding reconstruction with a minimal oversampling ratio," *IEEE Trans. Med. Imag.*, vol. 24, no. 6, pp. 799–808, Jun. 2005.
- [26] K. P. Pruessmann, M. Weiger, M. B. Scheidegger, and P. Boesiger, "SENSE: sensitivity encoding for fast MRI," *Magn. Reson. Med.*, vol. 42, no. 5, pp. 952–962, 1999.
- [27] B. Sutton, D. Noll, and J. Fessler, "Fast, iterative image reconstruction for MRI in the presence of field inhomogeneities," *IEEE Trans. Med. Imaging*, vol. 22, no. 2, pp. 178–188, Feb. 2003.
- [28] M. Zehni, L. Donati, E. Soubies, Z. Zhao, and M. Unser, "Joint angular refinement and reconstruction for single-particle cryo-EM," *IEEE Trans. Im. Proc.*, vol. 29, pp. 6151–63, 2020.
- [29] G. Wang, D. C. Noll, and J. A. Fessler, "Reconstruction may benefit from tailored sampling trajectories: optimizing non-Cartesian trajectories for model-based reconstruction," in *Proc. Intl. Soc. Mag. Res. Med.*, 2022, p. 5011. [Online]. Available: <https://submissions.miramart.com/ISMRM2022/Itinerary/Files/PDFFiles/5011.html>
- [30] K. Kreutz-Delgado, "The complex gradient operator and the CR-calculus," *arXiv preprint arXiv:0906.4835*, 2009.
- [31] J. R. Magnus and H. Neudecker, *Matrix differential calculus with applications in statistics and econometrics*. John Wiley & Sons, 2019.
- [32] A. Hjørungnes and D. Gesbert, "Complex-valued matrix differentiation: Techniques and key results," *IEEE Trans. Sig. Proc.*, vol. 55, no. 6, pp. 2740–2746, 2007.
- [33] M. R. Hestenes, "Multiplier and gradient methods," *J. Optim. Theory Appl.*, vol. 4, no. 5, pp. 303–320, Nov. 1969.
- [34] S. H. Chan, X. Wang, and O. A. Elgandy, "Plug-and-play ADMM for image restoration: fixed-point convergence and applications," *IEEE Trans. Computational Imaging*, vol. 3, no. 1, pp. 84–98, Mar. 2017.
- [35] H. K. Aggarwal, M. P. Mani, and M. Jacob, "MoDL: model-based deep learning architecture for inverse problems," *IEEE Trans. Med. Imag.*, vol. 38, no. 2, pp. 394–405, Feb. 2019.
- [36] S. Ramani and J. A. Fessler, "Parallel MR image reconstruction using augmented Lagrangian methods," *IEEE Trans. Med. Imag.*, vol. 30, no. 3, pp. 694–706, Mar. 2011.
- [37] J. A. Fessler, S. Lee, V. T. Olafsson, H. R. Shi, and D. C. Noll, "Toeplitz-based iterative image reconstruction for MRI with correction for magnetic field inhomogeneity," *IEEE Trans. Sig. Proc.*, vol. 53, no. 9, pp. 3393–402, Sep. 2005.
- [38] M. Lustig, D. L. Donoho, J. M. Santos, and J. M. Pauly, "Compressed sensing MRI," *IEEE Signal Process. Mag.*, vol. 25, no. 2, pp. 72–82, Mar. 2008.
- [39] M. J. Muckley, R. Stern, T. Murrell, and F. Knoll, "TorchKbNufft: A high-level, hardware-agnostic non-uniform fast fourier transform," in *ISMRM Workshop on Data Sampling & Image Reconstruction*, 2020.
- [40] O. Maier *et al.*, "CG-SENSE revisited: Results from the first ISMRM reproducibility challenge," *Magn. Reson. Med.*, vol. 85, no. 4, pp. 1821–1839, 2021.
- [41] R. D. Hoge, R. K. Kwan, and G. Bruce Pike, "Density compensation functions for spiral MRI," *Magn. Reson. Med.*, vol. 38, no. 1, pp. 117–128, 1997.
- [42] D. Kim and J. A. Fessler, "Adaptive restart of the optimized gradient method for convex optimization," *J Optim Theory Appl.*, vol. 178, no. 1, pp. 240–263, Jul. 2018.
- [43] J. A. Fessler, "Optimization methods for MR image reconstruction," *IEEE Sig. Proc. Mag.*, vol. 37, no. 1, pp. 33–40, Jan. 2020.
- [44] D. C. Noll, J. A. Fessler, and B. P. Sutton, "Conjugate phase MRI reconstruction with spatially variant sample density correction," *IEEE Trans. Med. Imag.*, vol. 24, no. 3, pp. 325–336, 2005.
- [45] M. Uecker *et al.*, "ESPIRiT - an eigenvalue approach to autocalibrating parallel MRI: where SENSE meets GRAPPA," *Mag. Reson. Med.*, vol. 71, no. 3, pp. 990–1001, Mar. 2014.
- [46] J. Zbontar *et al.*, "fastMRI: An open dataset and benchmarks for accelerated MRI," 2018. [Online]. Available: <http://arxiv.org/abs/1811.08839>
- [47] D. P. Kingma and J. Ba, "Adam: a method for stochastic optimization," 2017. [Online]. Available: <http://arxiv.org/abs/1412.6980>
- [48] A. Horé and D. Ziou, "Image quality metrics: PSNR vs. SSIM," in *Intl. Conf. on Patn. Recog. (ICPR)*, Aug. 2010, pp. 2366–2369.
- [49] C. Lazarus *et al.*, "SPARKLING: variable-density k-space filling curves for accelerated T2*-weighted MRI," *Mag. Res. Med.*, vol. 81, no. 6, pp. 3643–61, Jun. 2019.
- [50] C. Boyer, N. Chauffert, P. Ciuciu, J. Kahn, and P. Weiss, "On the generation of sampling schemes for magnetic resonance imaging," *SIAM J. Imaging Sci.*, vol. 9, no. 4, pp. 2039–2072, 2016.
- [51] F. Wajer and K. Pruessmann, "Major speedup of reconstruction for sensitivity encoding with arbitrary trajectories," in *Proc. Intl. Soc. Mag. Res. Med.*, 2001, p. 767.
- [52] H. Gu, B. Yaman, K. Ugurbil, S. Moeller, and M. Akcakaya, "Compressed sensing MRI with 11-wavelet reconstruction revisited using modern data science tools," in *Proc. Int'l. Conf. IEEE Engr. in Med. and Biol. Soc.*, 2021, pp. 3596–600.